

# Suitability of infrared microspectroscopic imaging for histopathology of the uterine cervix

Jens Einenkel,<sup>1,\*</sup> Ulf-Dietrich Braumann,<sup>2,3,\*</sup> Wolfram Steller,<sup>4,\*</sup> Hans Binder<sup>2</sup> & Lars-Christian Horn<sup>5</sup>

<sup>1</sup>Department of Obstetrics and Gynaecology, Centre for Women's & Children's Health, <sup>2</sup>Interdisciplinary Centre for Bioinformatics, <sup>3</sup>Institute for Medical Informatics, Statistics and Epidemiology, Leipzig University, Leipzig, <sup>4</sup>Institute for Analytical Chemistry, Dresden University of Technology, Dresden, and <sup>5</sup>Division of Perinatal and Gynaecologic Pathology, Institute of Pathology, Leipzig University, Leipzig, Germany

Date of submission 3 December 2010

Accepted for publication 4 June 2011

Einenkel J, Braumann U-D, Steller W, Binder H & Horn L-C

(2012) *Histopathology*

## Suitability of infrared microspectroscopic imaging for histopathology of the uterine cervix

**Aims:** Infrared microspectroscopy (IR-MSP) has been proposed for automated histological tissue differentiation of unstained specimens based on chemical analysis of cell and extracellular constituents. This study aimed to determine the accuracy of IR-MSP-based histopathology of cervical carcinoma sections with complex tissue architecture under practically relevant testing conditions.

**Methods and results:** In total, 46 regions of interest, covering an area of almost 50 mm<sup>2</sup> on sections derived from paraffin-embedded tissue of radical hysterectomy specimens, were analysed by IR-MSP (nominal resolution ~4.2 µm). More than 2.8 million pixel spectra that were processed using fuzzy c-means clustering followed by hierarchical cluster analysis permitted image segmentation regarding different biochemical properties.

Linear image registration was applied to compare these segmentation results with manual labelling on haematoxylin and eosin-stained references (resolution ~0.7 µm). For recognition of nine tissue types, sensitivities were 42–91% and specificities were 79–100%, mostly being affected by peritumoral inflammatory responses. Algorithmic variation of the outline of dysplasia and carcinoma revealed a spatial preference of false values in tissue transition areas.

**Conclusions:** This imaging technique has potential as a new method for tissue characterization; however, the recognition accuracy does not justify a pathologist-independent tissue analysis, and the application is only possible in combination with concomitant conventional histopathology.

**Keywords:** cervical cancer, computer-assisted image analysis, histopathology, infrared microspectroscopy

**Abbreviations:** FCM, fuzzy c-means clustering; FPA, focal plane array; FTIR, Fourier-transform infrared; H&E, haematoxylin and eosin; HCA, hierarchical cluster analysis; IR, infrared; IR-MSP, infrared microspectroscopy; PCA, principal components analysis; ROI, region of interest; SIMCA, soft independent modelling of class analogies

## Introduction

Infrared (IR) microspectroscopy (IR-MSP) is an emerging imaging technique providing molecular informa-

tion about metabolic and structural tissue status at high resolution. Such modern Fourier-transform infrared (FTIR) imaging systems, nowadays based on focal plane array (FPA) detectors combined with microscopic equipment, yield 'spectrum pixels' that locally represent the complex information referring to a certain spectral range of the electromagnetic waves. The spectral data can be analysed by univariate and multivariate spectrum pixel-related methods

Address for correspondence: J Einenkel, Zentrum für Frauen- und Kindermedizin der Universität Leipzig, Liebigstraße 20a, 04103 Leipzig, Germany. e-mail: jens@einenkel.eu

\*These authors contributed equally to this work.

(e.g. pattern recognition procedures, functional group mapping, and single-band analysis), and eventually provide simple arbitrarily coloured images without any staining procedure.<sup>1,2</sup> All of this appears to be ideal for an accurate, rapid, operator-independent and reproducible approach to characterize tissue sections, as has already been applied as a diagnostic tool for certain tissue probes.

The broad application field of IR-MSP-based histopathology has principally focused on the following clinical problem areas: (i) discriminating normal tissue from pathological or, particularly, malignant tissue alterations (e.g. screening methods and frozen sectioning);<sup>3–13</sup> (ii) analysing complex tissue architectures (to further objectify and specify visible light-based histopathological assessment);<sup>1,3,14,15</sup> (iii) localizing specific tissue components and biomarkers;<sup>16–19</sup> and (iv) evaluating biochemical variations within specific tissue types over time (functional assays).<sup>17,20</sup> Focusing on the first two mentioned areas, exciting results with very high values of accuracy have recently been reported for recognition of benign and malignant lesions in several tissues, including prostate, breast, pancreatic, oesophagus, brain and colon tissue.<sup>2–8</sup> However, previous studies have been limited in both their impact and their relevance concerning the number of analysed pixel spectra of the validation datasets. Some have remained below 1000,<sup>4,5,8,13</sup> and the majority of datasets have covered fewer than 500 000 spectra,<sup>3,9,11,12,15,18</sup> whereas regions of interest (ROIs) were, in part, restricted to well-defined areas.<sup>3,4,10,11</sup> Therefore, quality assessments of only small areas have raised the suspicion of a spatial-related selection bias.<sup>21</sup> A single study that analysed xenografted human colon carcinomas in a nude-mouse model comprised a very large dataset but did not determine the exact accuracy for tissue type recognition.<sup>22</sup> Furthermore, the approach of all previous studies was characterized by visual comparisons between IR-based segmentations and conventional histopathology, which represents the diagnostic 'gold standard'. This, however, means that real co-registration is missing, and this introduces an avoidable error that severely affects all further assessments. The successful translation of IR-MSP from a highly promising method for basic research to applications for clinical research and diagnostics clearly requires both more comprehensive and less restricted investigations.

Encouraged by previous spectroscopic studies on exfoliated cells from the uterine cervix<sup>23–25</sup> and promising results of IR spectral mapping of normal, dysplastic and neoplastic changes of human cervical tissue,<sup>26–28</sup> we have used radial uterine cervix tissue sections derived from patients with cervical cancer. For the first

time, we integrate both complete tissue segmentation of haematoxylin and eosin (H&E)-stained tissue sections and co-registration of IR-based and visible light-based images in order to precisely evaluate the accuracy of IR-MSP-based histopathology to an unprecedented extent.

## Materials and methods

### PATIENT CHARACTERISTICS, SAMPLE PREPARATION, WORKFLOW, AND MANUAL TISSUE SEGMENTATION

The study included a set of six randomly selected patients with cervical cancer who underwent total mesometrial resection,<sup>29</sup> a special type of nerve-sparing radical hysterectomy, with pelvic and possibly para-aortic lymphadenectomy as the primary treatment, at the Department of Obstetrics and Gynaecology, Leipzig University. The distribution according to pertinent clinical and histopathological variables is shown in Table 1. Tumours were classified according to the guidelines of the World Health Organization.<sup>30</sup> Informed consent to take specimens for research after clinical diagnosis was obtained.

The uterine cervix was opened lengthways, and radial samples were used to prepare adjacent pairs of 10- $\mu$ m-thick tissue sections. One was mounted on a conventional glass slide, stained with H&E, and imaged by transmission light microscopy. This first section served as a position reference and for identifying ROIs for IR microspectroscopy on the second section mounted on an IR-transparent calcium fluoride slide (Figure 1A,B). In addition, the slide was deparaffinized by washing in xylol and ethanol, according to the routine H&E staining procedure. After IR spectroscopic data were acquired, the section was also stained with H&E (Figure 1C). Photomicrographs with a nominal image resolution of  $\sim 0.7$   $\mu$ m per square pixel were recorded with a digital camera fitted to an inverse light microscope Olympus IX70 (Olympus, Hamburg, Germany).

A sample size of 46 ROIs covering a total area of 49.864 mm<sup>2</sup> was arbitrarily selected. ROIs were defined with the aim of capturing all tissue types of a respective section and, especially, for consideration of complex transition areas near tissue boundaries.

Histopathological assessment and manual tissue type segmentation of exactly the same ROIs (including small peripheral margins) were performed by a trained gynaecologic pathologist (L.-C.H.) in a blinded fashion with respect to the IR segmentation result. The image-editing software Corel Photo-Paint X3 (Corel, Ottawa, ON, Canada) was used to delineate the different tissue types, and the segmentation result was an

**Table 1.** Patient characteristics and morphological findings of all tumour specimens

Characteristic/feature	Patient/tumour					
	I	II	III	IV	V	VI
Age (years)	39	36	68	51	50	68
pT (tumour size and local spread)	1b1	1b2	2b	2b	2a	1b1
Tumour size (cm) (a/b/c)	2.5/3.0/2.2	4.9/4.0/3.6	2.7/3.6/1.3	5.2/4.0/2.5	2.7/2.5/0.9	2.0/2.0/0.5
pN (regional lymph nodes)*†	0 (0/48)	1 (3/34)	1 (1/35)	0 (0/34)	0 (0/59)	0 (0/43)
pM (metastases, distant lymph nodes)*†	X	0 (0/6)	0 (0/10)	X	X	X
Typing	Adenocarcinoma	SCC	SCC	SCC	SCC	SCC
Relative depth of cervical stroma invasion (%)	100	100	100	100	100	73
Grading	3	2	3	1	2	2
L (lymph vascular space involvement)*	1	1	1	1	1	1
V (blood vascular space involvement)*	0	0	0	0	0	1
Pattern of invasion	Finger-like	Finger-like	Closed	Finger-like	Diffuse	Closed
Peritumoral inflammatory response	Strong	Weak	Strong	Weak	Weak	Strong

SCC, Squamous cell carcinoma.

\*X = Not known; 0 = no; 1 = yes.

†Number of positive nodes/number of all removed nodes.

inconsistency-free label image depicted with false colours (Figure 2A,B). The distribution of a total of nine distinct tissue types is summarized in Table S1. If staining-caused deformations of the second section previously used for IR-MSP were too pronounced, the adjacent section used for position reference was instead taken for manual segmentation in 24% of all 46 ROIs ( $n = 11$ ; see highlighted values in Table S2).

#### IR-MSP DATA ACQUISITION AND PREPROCESSING

IR spectra were recorded with a Bruker IFS66/S FTIR spectrometer coupled to a Hyperion microscope and equipped with a  $64 \times 64$  FPA detector (Bruker Optik, Ettlingen, Germany). Images of 4096 IR spectra at a spectral resolution of  $8/\text{cm}$  were acquired with Opus software (Bruker), with the FPA operated in continuous-scan mode by co-adding 21 interferograms. Nominal coverage of a single FPA detector element corresponds to a tissue area of  $4.2 \times 4.2 \mu\text{m}^2$  at

$\times 15$  magnification. If the ROI area exceeded  $267 \times 267 \mu\text{m}^2$ , a series of IR images were recorded by moving the sample stage in increments of  $267 \mu\text{m}$  (mapping approach).

Data pretreatment included the merging of different IR images into a single dataset, filtering, baseline correction, and normalization. A spectral range from  $950$  to  $1800/\text{cm}$  was captured, and to discriminate between different tissue types, a reduced range from  $950$  to  $1480/\text{cm}$  was considered as a fingerprint region. Different backgrounds and offsets in the spectra were corrected by subtracting a linear baseline over the considered ranges. Low-absorbance spectra with poor signal-to-noise ratios were removed from further analysis ('reject' cluster no. 13). The spectra were further scaled at the amide I band ( $1655/\text{cm}$ ) to obtain relative intensities between zero and unity by multiplying by a correction factor. This normalization is assumed to compensate for the effect of global intensity changes resulting from slight variations in sample thickness.

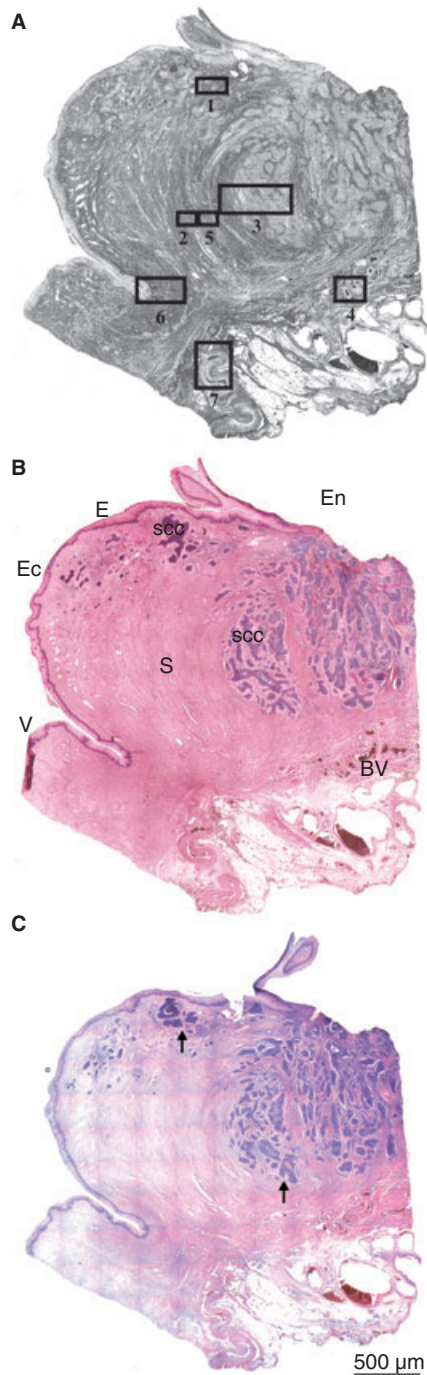


**Figure 1.** Microscopic overview of images of two neighbouring sections of tumour II. A, Unstained section mounted on a  $\text{CaF}_2$  window with labelling of seven regions of interest (ROIs) (the size of each region is given in Table S2). B, Adjacent section of A/C stained with haematoxylin and eosin (H&E) for primary determination of the ROIs. Ec, ectocervix; En, endocervix; V, vagina; E, epithelium; SCC, squamous cell carcinoma; S, stroma; BV, blood vessels filled with erythrocytes. C, Section A was stained with H&E after infrared data acquisition; arrows indicate regions with clear differences in relation to the adjacent section B (section-to-section variations).

#### SEGMENTATION OF THE IR IMAGES

The applied two-stage segmentation was performed by the analytical chemist (W.S.) in a blinded fashion, and utilized a combination of unsupervised and supervised pattern recognition methods. The first bootstrapped the second; that is, reference data for parameterization in the final supervised step were gained from the preceding unsupervised step. Whereas the latter was accomplished with our previously described approach consisting of non-hierarchical fuzzy c-means clustering (FCM) following a hierarchical cluster analysis (HCA),<sup>1</sup> here a supervised classification scheme called soft independent modelling of class analogies (SIMCA) was applied. SIMCA was considered for this work because the FCM/HCA method alone is no longer feasible, owing to the quadratic complexity of computer memory requirements, and would demand the complete set of spectra to be clustered. However, SIMCA requires training data, which in turn can be provided by using FCM/HCA, as long as the underlying data amount remains restricted. Direct access to training data is not possible, as histological characterization would necessitate procedures adversely affecting any following IR-MSP processing.

In detail, unlike HCA, FCM clustering is feasible for large spectra numbers. HCA, however, provides clustering results with explicit similarity distance information. Therefore, after pre-clustering the data into 35 clusters (far beyond the expected number of tissue types), in the HCA step the number of FCM clusters was further restricted to 12, to roughly agree with the number of present tissue types, as was suggested after initial histopathological assessment of the microscopic images. This FCM/HCA cascade for providing the training data for SIMCA was applied to a subset of the ROIs with  $\sim 0.5 \times 10^6$  spectra.

To perform the training for SIMCA, from this subset of spectra about 4500 model spectra, together with their corresponding cluster labels 1–12 assigned by FCM/HCA, were extracted. The main criterion for selecting model spectra was to reflect the spectral diversity observed for each of the 12 FCM/HCA pre-clustered regions, whereas the resulting number of contributing spectra remained between 200 and 1000 per cluster. The basic principle of SIMCA is to accomplish a separate principal components analysis (PCA) for the spectral data contributing to each cluster. Therefore, cluster-individual PCA models represented by a linear subspace around a mean vector were obtained from the training phase. In the application phase of the SIMCA method, the vectorial distance between a sample and each PCA model was computed

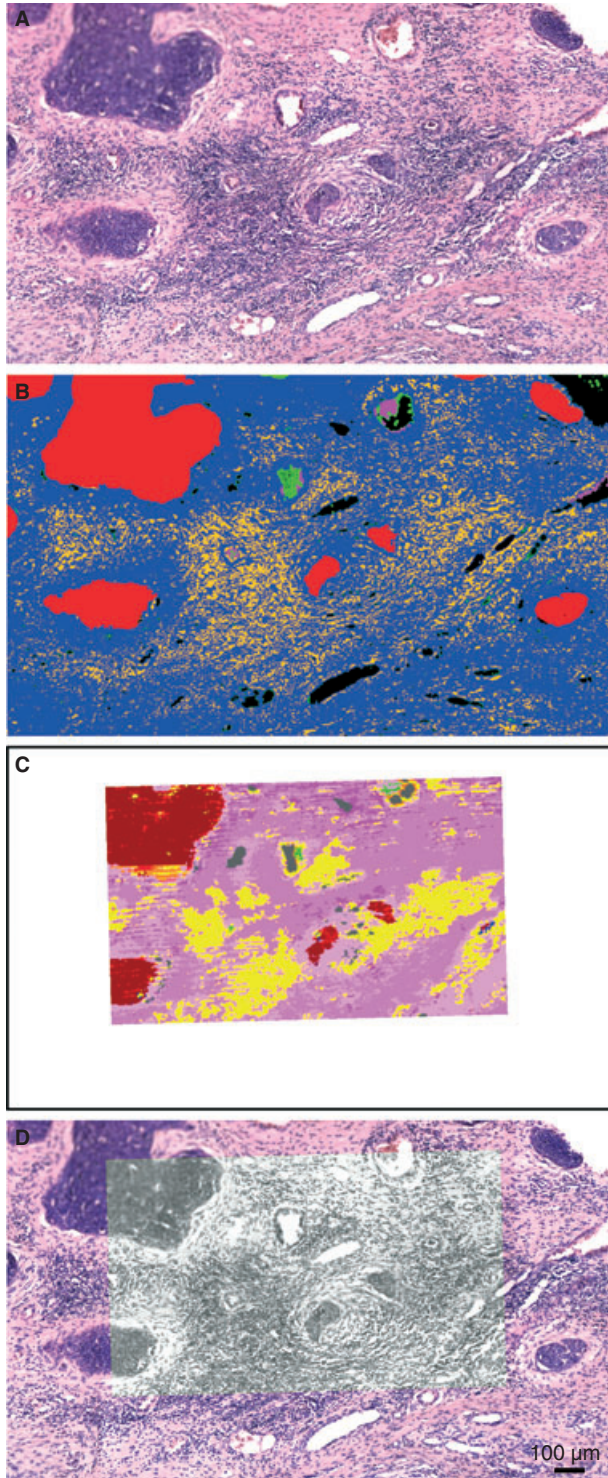


**Figure 2.** Region of interest (ROI) no. 1 of patient/tumour II (see Figure 1). A, Microscopic image of the haematoxylin and eosin (H&E)-stained section ( $0.66 \times 0.66 \mu\text{m}^2/\text{pixel}$ ). B, Complete manual segmentation of the H&E-stained image A with six tissue classes: red, tumour; blue, cervical stroma; yellow, inflammatory cells; magenta, erythrocytes; green, mucus and detritus; black, holes and fissures. C, Infrared microspectroscopy (IR-MSP) image of a part of the same tissue section taken before staining and scaled on the same size (lower resolution of  $4.2 \times 4.2 \mu\text{m}^2/\text{pixel}$  spectra); the colours represent 12 IR clusters. D, Alignment of the infrared and H&E images after registration (scaling, translation, and rotation) based on four manually assigned orientation points; the image analyses yielded the following values of sensitivity and specificity: 91.1% and 98.9% for the areas of squamous cell carcinoma; 80.5% and 58.1% for stroma; 37.0% and 85.2% for inflammatory cells; and 16.0% and 99.9% for erythrocytes.

visualize the clustering results, coloured label images were provided, indicating respective regions with similar spectral absorption properties (Figure 2C).

#### IMAGE REGISTRATION AND EVALUATION OF IR TISSUE RECOGNITION

To objectively compare the segmentation results obtained from the IR chemical with dye-assisted imaging, an intermediate step was required to co-register the images of both modalities. An interactive landmark-based linear (rigid) image registration was applied, whereby a redundant number of four respective landmark points was assigned for each image pair. A least-squares fitting procedure was applied in order to determine the registration parameters. Solutions for scaling, rotation and translation to accomplish the registration can be directly computed. The reference image geometry was set to that of the histological images; that is, the nominal pixel size for performance of one-by-one comparisons was approximately  $0.7 \times 0.7 \mu\text{m}^2$ . This rigid registration and the adaptation of resolution were applied to all 46 ROI pairs, and finally the coincidence of the IR-based segmentation results and the manual labelling of the H&E-stained sections was determined pixel by pixel (Figure 2D).

#### TUMOUR SEGMENT OUTLINE VARIATION EXPERIMENT

Preliminary investigations have suggested the assumption that transition areas of adjacent tissue types are problematic and represent the major error source in IR-MSP tissue recognition.<sup>21</sup> The impact of these transition areas on the accuracy of IR-MSP was estimated by an algorithmic variation of the outline of dysplasia and carcinoma segments in the histopathological reference in relation to an IR cluster combination (cluster combination synonym 'atypical tissue no. 2'; see

after projecting the sample spectra data into each respective linear subspace. The model with the closest distance was considered to best represent the spectrum of the sample, so that its physical area (i.e. the IR pixel) could finally be assigned to a certain IR cluster. To

Results). Starting from the original result of the manual tissue type segmentation, the segment outlines were varied stepwise ( $n = 15$ ) in the following way: in order to determine the alteration of sensitivity, the outline was shrunk, and to assess the specificity, the outline was enlarged (Figure 3).

#### STATISTICAL ANALYSIS

Data analysis was primarily descriptive. Sensitivity and specificity statistics were used to evaluate IR-MSP imaging as a diagnostic test for the recognition of different tissue types. The terms true and false refer to the histological reference regarding the presence or absence of the tissue type of interest. Sensitivity is the proportion of true-positive spectra pixels of all pixels of the pertaining tissue type; specificity is the proportion of true-negative pixels of all pixels of the remaining tissue types. For easy comparison of these values between histopathologically defined subgroups, 'accuracy', defined as a proportion of both true positives and true negatives in relation to all, was additionally used. Features measured in continuous scales were summarized in box-and-whisker plots, and categorical features were presented as counts and proportions. The Wilcoxon test was used for the analysis of paired values that were not normally distributed.

## Results

#### MATCHING MATRIX FOR MICROSPECTROSCOPIC AND HISTOPATHOLOGICAL IMAGING

All 46 ROIs of the validation dataset were composed of a total number of 2 864 960 spectra pixels. Subsequently, the H&E-stained sections were digitalized at a higher spatial resolution, which resulted in 108 044 942 image pixels for the same overall area (resulting scaling factor: 6.14).

The basis for differential assessments of the results obtained is provided by the histology-related matching matrix (Table 2). The maximum values of coincidence between the different tissue types and all IR clusters ranged from 35% to 80%, with the highest coincidence between 'blood vessels' and cluster 6. The worst maximum values were found for 'mucus and detritus' (IR cluster 8) and 'glandular epithelium' (IR cluster 6). Pixels of the former also showed a high level of coincidence (27%) with the '13th cluster', representing a rejection class either for spectra arising from tissue-free areas or spectra with poor signal-to-noise ratios. Mucus and cell detritus were localized within hollows, glandular ducts and tissue-free areas, exhibiting

only low diagnostic importance. Glandular epithelium showed a flat frequency distribution over three IR clusters (6–8). Some other tissue types were ambiguously represented by several IR clusters, which were expediently combined for further analysis. In order to achieve an unambiguous assignment between one tissue type and several IR cluster combinations, 'cluster combination synonyms' were introduced (Table 3, column 3).

#### TISSUE TYPE-RELATED ASSESSMENT OF ACCURACY BY BINARY CLASSIFICATION TESTING AND ITS VARIATION BETWEEN THE DIFFERENT ROIS

Considering all patients, values of sensitivity and specificity ranged from 46% to 91%, and from 79% to 100%, respectively, for recognition of the different tissue types (Table 3). In spite of possible IR cluster combining, glandular epithelium was not reasonably assignable. Although its maximum match occurred for IR cluster 6 (peak: 35%), this cluster 6 in turn was also well associated with stroma and blood vessels and, in fact, it would be better included in a cluster combination {4, 5, 6} associated with both stroma and vessels (Table 2). This can clearly be attributed to the fact that this glandular epithelium consists of a stroma-adjacent cellular monolayer with a thickness in the order of the spatial resolution of IR-MSP (Figure 4). Unfortunately, this finding emphasizes that some relevant histological structures with extents too close to the diffraction limit may possibly be missed.

If the sensitivity and specificity are calculated not only for the whole dataset, but separately for each ROI, the values show a considerable variance, as is demonstrated in the box-and-whisker plot in Figure 5.

In all cases where the adjacent section had to be used for segmentation, the test accuracy was not worsened (e.g. 92.9% versus 92.8% for recognition of atypical tissue no. 2; Table 4).

#### ERROR ANALYSIS OF THE CLASSIFICATION RESULTS

The tissue types 'stroma' and 'inflammatory response' were most frequently classified as 'false positive' in the sensitivity and specificity statistics (Table 3, rightmost column). This outcome concerning 'stroma' was expected; stroma represents the dominantly occurring tissue type of the whole dataset (57%; Table S1), has a key tissue-supporting function, and occurs adjacent to most other tissues. Furthermore, the 'inflammatory response', i.e. the infiltration of tissue with inflammatory and immunocompetent cells, is not an actual

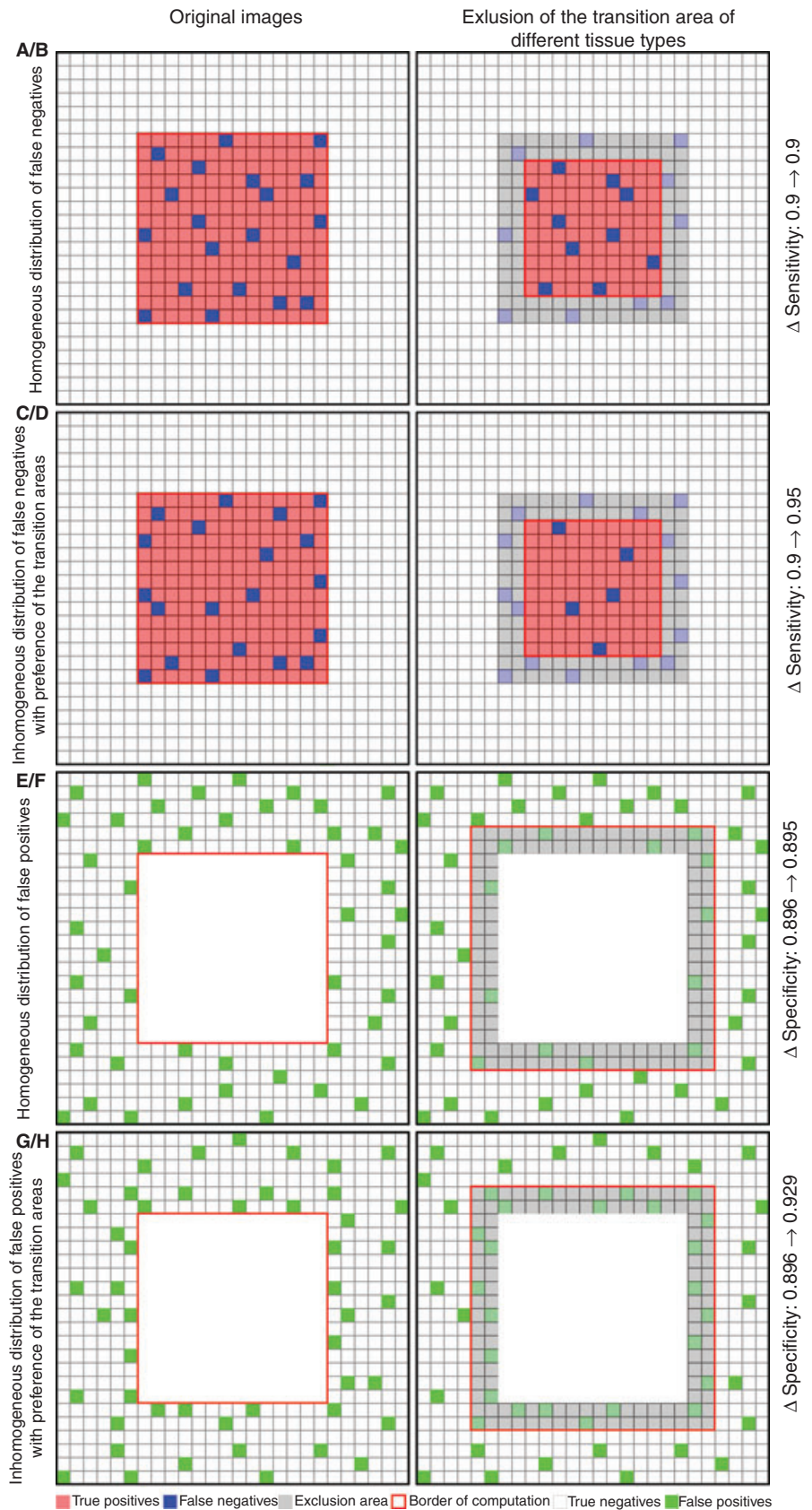


**Figure 3.** Schematic representation of two possible changes in sensitivity (A/B,C/D) and specificity (E/F,G/H) at a time as a function of the size of the region of interest (ROI) and the distribution of false negatives and false positives, respectively. In the case of the preference of false negatives and positives in the transition area of different tissue types, exclusion of this area yields a distinct increase in sensitivity and specificity (C/D,G/H). There is no change in these values if the size of the ROIs is reduced for a homogeneous distribution of both false negatives and false positives (A/B,E/F).

**Table 2.** Matching matrix. The data value at any matrix position is a fraction of pixels (%; sensitivity) of a histologically classified tissue type (row sum = 100%); each tissue type is represented by a combination of different fractions of the 13 infrared (IR) clusters; assignment of IR clusters to definite tissue types (as shown in Table 3) is based on the distribution of these values (the number of pixels of each tissue type is given in Table S1)

True tissue type	IR cluster												
	1	2	3	4	5	6	7	8	9	10	11	12	13
Stroma	1.20	0.94	0.58	21.85	<b>38.02</b>	22.06	12.40	0.38	0.03	0.01	0.05	0.33	2.15
Epithelium	1.07	2.43	7.57	0.02	0.06	1.21	1.43	<b>51.90</b>	27.85	3.08	0.00	0.00	3.38
Inflammatory response	2.24	3.04	1.43	2.93	10.52	12.34	<b>66.17</b>	0.42	0.05	0.01	0.00	0.04	0.82
Glandular epithelium	3.77	1.12	2.37	1.03	2.36	<b>35.26</b>	23.91	21.42	1.30	0.00	0.00	0.00	7.46
Blood vessels	0.00	0.00	0.00	5.40	7.66	<b>79.96</b>	4.23	0.95	0.00	0.00	0.32	0.05	1.43
Erythrocytes	0.02	0.05	0.01	2.14	0.84	12.35	6.48	4.92	0.00	0.00	11.89	<b>50.48</b>	10.82
Mucus, detritus	4.82	1.37	0.74	1.12	1.35	19.19	8.67	<b>34.86</b>	0.46	0.00	0.18	0.47	26.77
Dysplasia	7.28	<b>74.44</b>	5.93	0.17	0.01	1.00	6.77	1.19	0.65	0.00	0.00	0.00	2.56
Dysplasia/carcinoma*	<b>57.93</b>	32.00	0.76	0.01	0.00	0.80	6.79	0.71	0.32	0.00	0.00	0.02	0.66
Carcinoma	<b>45.72</b>	22.49	4.08	0.34	0.14	6.40	17.33	0.98	0.33	0.00	0.00	0.00	2.19
Shrinkage artefacts	1.73	1.16	0.15	18.18	9.17	8.90	8.03	6.22	0.25	0.00	0.45	2.80	<b>42.97</b>

\*Not possible to differentiate by the pathologist.

Bold type indicates the maximum value in each row.

tissue type from the classical point of view, but is a frequent and important histopathological feature. The dependence of test accuracy on the degree of inflammatory response is demonstrated in Figure 6 for the recognition of 'atypical tissue no. 2'.

#### TISSUE SUBTYPE HETEROGENEITY AND CORRELATION WITH MORPHOLOGICAL TUMOUR FEATURES

The number of clusters was chosen to be slightly higher than that of the correspondingly defined histological tissue types, so that 'chemical tissue entities' that appear to be possibly morphologically identical could potentially be differentiated. Thereby, the potential for structure-related subdifferentiation was investigated by visual assessment of those histopathological tissue types obviously represented by two or more IR clusters, in order to find preferences in topology. Only in the case of squamous epithelium were good structural correspondences found, for three detected sublayers represented by the IR clusters 8, 9, and 10. However, similar in-depth analyses of stroma, atypical tissue and erythrocytes did not yield a morphologically identifiable preference of IR cluster localization within the tissues

when compared with corresponding H&E-stained sections.

The influence of several histopathological tumour-related features (typing, grading, pattern of invasion, etc.) on accuracy was evaluated for atypical tissue (dysplasia and carcinoma; IR cluster combination synonym 'atypical tissue no. 2'; Table 3). The largest difference in accuracy between the various feature stages was <8% points (Table 4). Interestingly, for poorly differentiated tumours (grading G3), as well as for tumours with a closed invasion front pattern, the lowest recognition accuracy was measured (about 88%), but a more in-depth analysis of these data was not indicated, owing to the limited number of cases.

#### TUMOUR SEGMENT OUTLINE VARIATION EXPERIMENT

Exclusion of transition areas was accompanied by increases in both sensitivity and specificity (Figure 7). The paired comparison of sensitivity and specificity values by use of the Wilcoxon test demonstrated a significant difference between each step  $n$  and  $n + 1$  (sensitivity,  $P \leq 0.003$ ; specificity,  $P \leq 0.00002$ ). The increase in these values substantiates the spatial

**Table 3.** Characteristics of infrared (IR) spectroscopy as diagnostic test for recognition of histological tissue types with regard to all patients; cluster combination synonyms in bold type are further illustrated in Figure 5

True tissue type	IR cluster no.	Cluster combination synonym	Sensitivity (%)	Specificity (%)	Both tissue types with the most frequent false-positive assignment
Stroma	4, 5, 6	Stroma	81.9	80.6	Shrinkage artefacts, inflammatory response
Blood vessels	6	Blood vessels	80.0	84.0	Stroma, inflammatory response
Stroma and blood vessels	4, 5, 6	<b>Stroma and blood vessels</b>	<b>82.2</b>	<b>83.4</b>	Shrinkage artefacts, inflammatory response
Epithelium	8, 9, 10	<b>Epithelium</b>	<b>82.8</b>	<b>98.4</b>	Shrinkage artefacts, Mucus, detritus
Inflammatory response	7	<b>Inflammation</b>	<b>66.2</b>	<b>88.2</b>	Stroma, carcinoma
Erythrocytes	11, 12	<b>Erythrocytes</b>	<b>62.4</b>	<b>99.5</b>	Shrinkage artefacts, Stroma
Dysplasia	2	Dysplasia	74.4	95.2	Carcinoma, dysplasia/carcinoma
Carcinoma	1	Carcinoma	45.7	97.2	Dysplasia/carcinoma, Stroma
Dysplasia and carcinoma	1, 2	Atypical tissue no. 1	71.9	97.4	Stroma, inflammatory response
Dysplasia and carcinoma	1, 2, 3	<b>Atypical tissue no. 2</b>	<b>75.8</b>	<b>96.4</b>	Stroma, inflammatory response
Dysplasia and carcinoma	1, 2, 3, 7	Atypical tissue no. 3	91.0	79.4	Stroma, Inflammatory response
Mucus, detritus, and shrinkage artefacts	'13'	Detritus	41.7	97.8	Stroma, carcinoma

preference of false negatives and false positives in the transition area (Figure 3C,D,G,H).

## Discussion

Both H&E staining-based classical histopathology and IR-MSP-based biochemical histopathology are sophisticated pattern recognition methods; however, they operate on different levels. Whereas IR-MSP assesses patterns in the high-dimensional pixel spectra, conventional histopathology is based on comparatively low-dimensional colour perception, and considers locally extended structural patterns obtained at a higher level of detail. A comparative analysis of both methods assumes that, for IR-MSP, slight cell differences concerning concentration and conformations of functional groups associated with proteins, lipids, nucleic acids and carbohydrates are distinctive enough for recognition of specific tissue types.

## ASSESSMENT OF THE METHODOLOGICAL APPROACH

To meet the requirements of conventional histopathology, practically relevant investigation conditions, such as the use of formalin-fixed paraffin-embedded tissue samples, large ROIs with transition areas on tissue boundaries, simultaneous recognition of all tissue types (possibly with strongly varying portions), and a high level of detail, are needed in the study design. Our approach comes close to these requirements, as follows.

The fixation and the impregnation of the specimens with the embedding paraffin followed by deparaffinization is accompanied by obvious, and so far not completely evaluated, changes in the molecular tissue characteristics, and by the possibility that residual paraffin could impair the spectroscopic data.<sup>31</sup> However, the advantages of the approach outweigh the problems with the fresh frozen section technique, so that it has been used by most of the published studies.

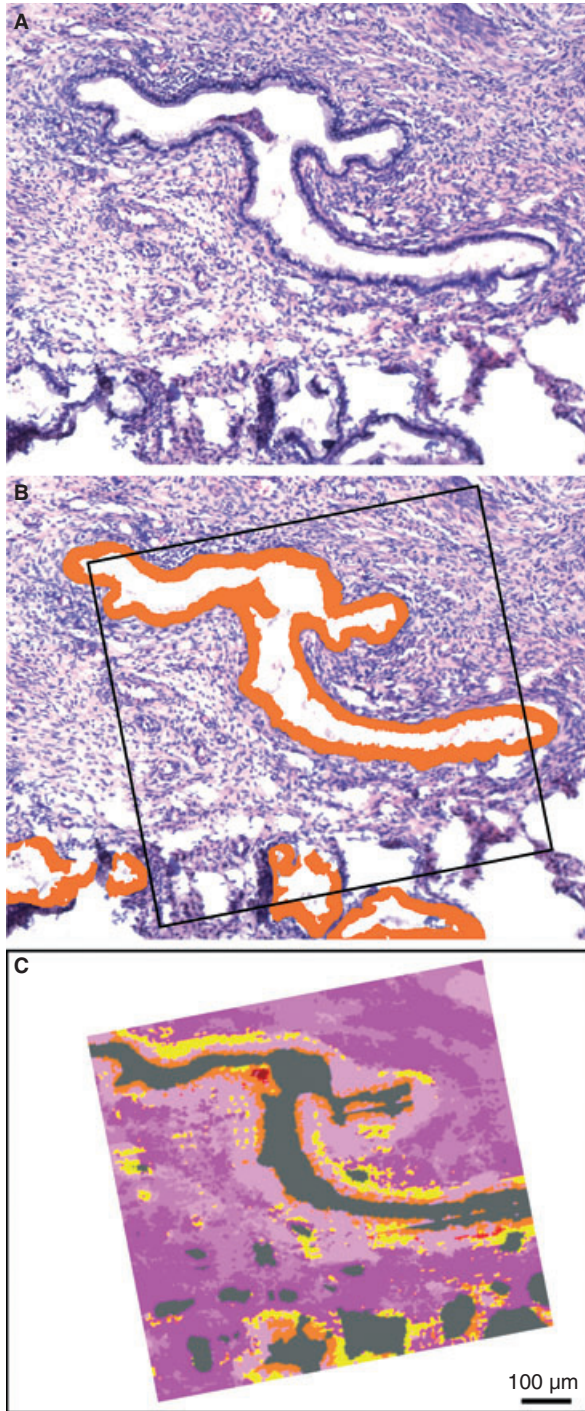


**Figure 4.** Infrared (IR) microspectroscopy (IR-MSP)-based segmentation of glandular epithelium. A, Haematoxylin and eosin-stained microphotograph of a region of interest (ROI) of tumour VI. B, Glandular epithelium is manually segmented and labelled orange; the result of image registration is denoted by a rectangle. C, Corresponding IR-MSP image; IR cluster 6 is also shown in orange; despite the uninterrupted epithelial layer in A, cluster 6 looks like a discontinuous streak; values of sensitivity, specificity and accuracy are 43.1%, 84.6% and 79.2%, respectively, for this isolated ROI.

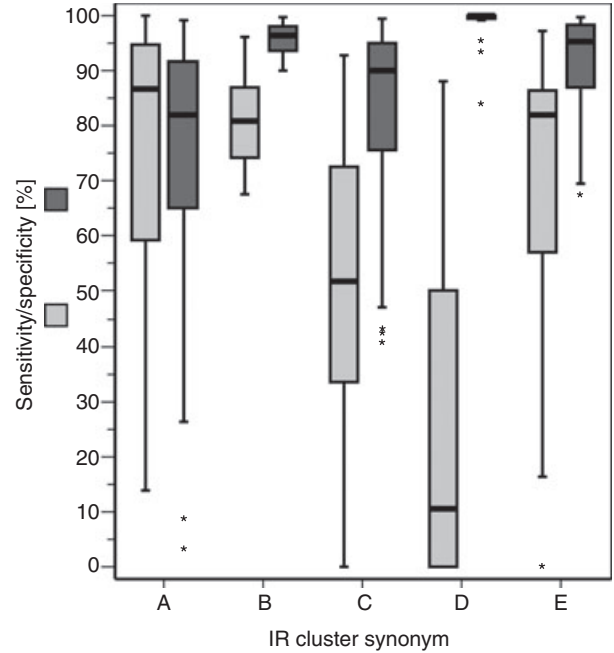


**Figure 5.** Variation in sensitivity and specificity for selected infrared cluster combination synonyms (see Table 3) computed for each region of interest containing the considered tissue type. A, 'Stroma and blood vessels' ( $n = 46$ ). B, 'Epithelium' ( $n = 8$ ). C, 'Inflammation' ( $n = 34$ ). D, 'Erythrocytes' ( $n = 26$ ). E, 'Atypical tissue no. 2' ( $n = 22$ ). \* Outliers

Notably, direct analysis of paraffin-embedded specimens without prior chemical dewaxing is also possible.<sup>18,22</sup>

The average size of the 46 ROIs analysed in our study was  $1.084 \text{ mm}^2$ , which considerably exceeds the areas of ROIs of previous studies, particularly if they used tissue microarrays to prepare the slides. The standard diameter of punches is  $0.6 \text{ mm}$ , resulting in an area of  $0.283 \text{ mm}^2$ .<sup>3</sup> Evidently, restricting the analyses to very small selected areas is not appropriate for evaluation of IR-MSP as a technique for general histopathology.

Spatial resolution is a critical measurement parameter in IR-MSP, and strongly affects the character of the IR spectral data. The high lateral spatial resolution obtained in our IR imaging setup corresponds with previously published analyses indicating a resolution of approximately  $4\text{--}10 \text{ }\mu\text{m}$ . A real improvement in resolution cannot be achieved with currently available IR-MSP equipment, because these values are near the diffraction limit (first realized by Abbé) in the mid-IR region. Possibly, future developments, such as new near field imaging techniques, might overcome this problem.

An important step in our processing chain is the pairwise rigid image co-registration employed for all

**Table 4.** Recognition of atypical tissue (see Table 3; 'atypical tissue no. 2': dysplasia and carcinoma) stratified according to different histopathological features and the relationship of haematoxylin and eosin (H&E) and infrared (IR) specimen sections based on IR clusters 1, 2, and 3

Stratification feature	Patient/tumour (ROI no.)	Total size of H&E images (pixels)	Sensitivity (%)	Specificity (%)	Accuracy (%)
Typing					
SCC	II, III, IV, V, VI	93 324 099	76.2	96.3	92.5
Adenocarcinoma	I	14 720 843	69.5	97.0	95.0
pN					
pN0	I, IV, V, VI	66 936 310	85.1	95.4	93.5
pN1	II, III	41 108 632	56.9	97.8	91.7
Grading					
G1	IV	18 592 725	92.2	89.9	90.7
G2	II, V, VI	61 481 126	81.3	97.6	95.4
G3	I, III	27 971 091	35.2	96.9	88.6
Blood vascular space involvement					
V0	I, II, III, IV, V	95 914 517	75.3	96.3	92.6
V1	VI	12 130 425	80.8	96.8	94.4
Pattern of invasion					
Closed	III, VI	25 380 673	45.3	96.7	87.7
Finger-like	I, II, IV	61 171 952	87.6	95.9	94.4
Diffuse	V	21 492 317	78.0	97.2	94.5
Peritumoral and intratumoral inflammatory response					
Weak	II, IV, V	67 943 426	86.8	96.1	94.3
Strong	I, III, VI	40 101 516	50.0	96.8	90.4
Relationship between H&E and IR specimen sections					
Same section	I (1, 6), II, III, IV (1, 7), V, VI (1-6, 8-10) ( <i>n</i> = 35)	81 400 290	71.0	96.9	92.9
Adjacent sections	I (2-5), IV (2-6), VI (7, 11) ( <i>n</i> = 11)	26 644 652	86.4	94.6	92.8

SCC, Squamous cell carcinoma.

ROIs to find an optimum of the pixel coincidence of both modalities. The compensation for deformations caused by the staining procedure and by differences in the adjacent section (in one-quarter of cases) was referred to the total area of an ROI. Treating partial deformations would have required non-rigid co-registration, a complex procedure necessitating a large and unavailable number of corresponding landmark points. Otherwise, a simple visual comparison of both IR chemical and dye-assisted imaging is not accept-

able for studies characterized by precise statistical analysis.

#### ASSESSMENT OF THE RESULTS OBTAINED

The obtained values of sensitivity and specificity associated with the limited recognition/identification of small structures (e.g. glandular epithelium) and the considerable variance between ROIs of different localization were both surprising and disappointing, and

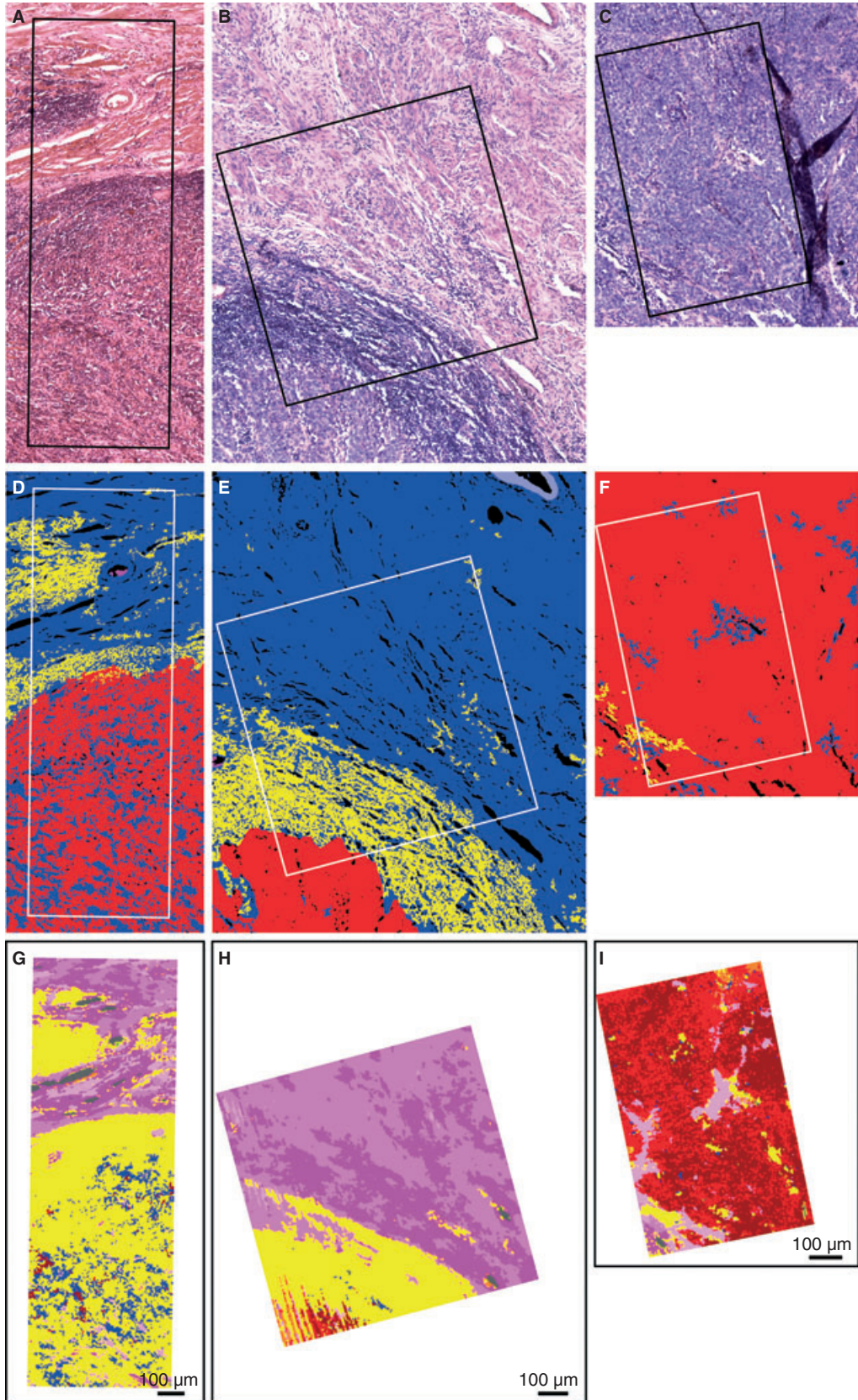


**Figure 6.** Different levels of accuracy for histopathological recognition of tumour areas of squamous cell carcinomas derived from tumour III [region of interest (ROI) 4; left column) and tumour VI (ROIs 6 and 9; middle and right column; see Table S2). A–C, Microphotographs of haematoxylin and eosin (H&E)-stained 10- $\mu\text{m}$  tissue sections of the cervix uteri with rectangle labels of the ROIs. D–F, Images of complete manual segmentation by the pathologist with six classes: red, squamous cell carcinoma; blue, cervical stroma; light blue, vessel wall; yellow, inflammatory response; magenta, erythrocytes; black, holes and fissures. G–I, Infrared microspectroscopy images of the ROIs at the same scale as the H&E images. For recognition of tumour areas (atypical tissue no. 2, see Table 3), difference image analysis yielded a sensitivity of 16.4% and a specificity of 95.1% for tumour number III, characterized by dissociative growth and strong peritumoral tissue infiltration of inflammatory cells (G). The sensitivity and specificity of ROIs 6 and 9 of tumour VI were 38.8% and 99.5%, and 86.5% and 69.5%, respectively. The clear difference in test accuracy for the same specimen is caused by different proportions of tumour and peritumoral and intratumoral inflammatory responses.

may represent objections to the use of IR-MSP as an objective, unsupervised and unbiased clinical application in histopathology. In our opinion, IR-MSP remains a complementary tool, to be used in combination with conventional histopathology and immunohistochemistry. In particular, the high number of spectra pixels, the large ROIs including very complex tissue areas and the newly introduced image co-registration substantiate our final assessment of the method, in contrast to many

studies cited in the Introduction, which received very favourable appraisals. Really promising publications in recent years indicating very high resolution and important clinical relevance, such as the detection of micrometastases in lymph node histopathology or the analysis of already stained cell preparations (cytospin and smear), are very impressive, but their methodical approach is characterized by a low number of mostly selected samples.<sup>11,15,32</sup>

Regarding our study, there is only a very small chance that a further increase in the number of patients or an enlargement of the size of ROIs could considerably improve the accuracy. The main source of trouble found in our analysis is the infiltration of tissue with inflammatory and immunocompetent cells associated with changes in the extracellular matrix resulting from protein accumulation. This kind of cellular and non-cellular disturbance of the tissue homogeneity directly causes spectral mixing, and thus makes IR-MSP analysis unreliable in those regions. A similar result was found by the analysis of confounding variables in the microspectroscopic assessment of Pap smears, where leukocytes and, in particular, lymphocytes misleadingly had spectral features suggestive of changes indicative of malignancy.<sup>33</sup>

In addition to local tissue inflammation, the accuracy of IR-MSP might be affected by further important aspects that are frequently encountered in solid tumours. For example, the metabolic status of a tumour is heterogeneous with regard to different areas, depending on the availability of oxygen and nutrients, and chemical tumour tissue composition might therefore be influenced by further unpredictable components within the cells and the extracellular matrix.<sup>17</sup> Furthermore, tumours derived from one and the same tissue type may show considerable morphological heterogeneity, and may appear with several histological subtypes (cellular origin and differentiation) and grades (nuclear differentiation). Our proof-of-concept study demonstrates a minor influence of several histopathological tumour-related features on the accuracy of recognition of dysplastic and carcinomatous tissue. The influence of those features seems to be insignificant

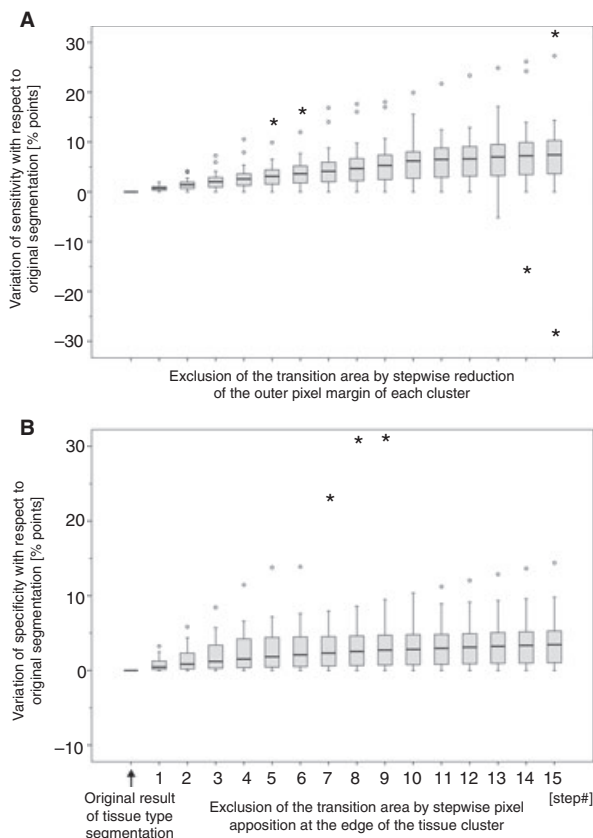


**Figure 7.** Variations in the sensitivity (A) and specificity (B) statistic for the infrared cluster combination synonym 'atypical tissue no. 2' induced by a layer-by-layer pixel reduction (A) respectively apposition (B) (15 steps) of the tissue areas dysplasia and carcinoma (theoretical background is given in Figure 3). The analysis is based on 22 regions of interest (ROIs) of all tumours (dots and asterisks are outliers and extremes).

if compared with the high variance resulting from the localization of separately calculated ROIs (Figure 5). Only a few analyses concerning such detailed morphological assessment have been published so far. An interesting study, however, characterized by a small number of spectra, examined samples of benign endometrial tissue and several subtypes of endometrial carcinoma/sarcoma (endometrioid, serous papillary and malignant mixed Müllerian tumours).<sup>13</sup> The separation between spectra derived from different subtypes was good, and, additionally, depending on the presence of antecedent tamoxifen usage, separation was dramatically improved. Unfortunately, precise values of the sensitivity and specificity statistics were not given.

The subdifferentiation of tissue types revealed a distribution of three IR clusters in accordance with the layer-related cell differentiation of squamous epithelium; these have already been demonstrated in previous studies, and were mainly related to glycogen and nucleic acid bands.<sup>1,26,28</sup> Our previous analysis has shown that a still more detailed hierarchical classification of the IR data allows further segmentation of all morphologically deducible cell layers.<sup>1</sup> Furthermore, a recently published study that analysed uterine cervical samples of exfoliated cells by IR-MSP (referred to as 'spectral cytopathology') actually detected cellular abnormalities in spectral characteristics of morphologically normal-appearing cells.<sup>34</sup> The observed discrete biochemical changes were interpreted as being probably caused by infection with human papillomavirus. The same trends were observed in another study of oral mucosa cells, in which morphologically normal epithelial cheek cells infected with herpes simplex virus were characterized by cell changes that were only spectroscopically detectable.<sup>35</sup> Unfortunately, the quoted studies are limited in their impact, because of the very low number of samples and the restrictive inclusion criteria.

With regard to oncological issues, recent studies have demonstrated marked heterogeneity of tumour tissue, as well as the secreted mucus, that is undetectable by conventional histological staining.<sup>18,22</sup> Our analysis confirms the possibility of using IR-MSP to characterize spectral subtypes of tumour tissue (IR clusters 1–3), but the interpretation of this finding is very complex. All of these studies make it obvious that IR-MSP has the potential to track biochemical variations in cells and tissues that are not associated with visible morphological changes, and, therefore, the intended subdifferentiation of tissue types should be based not only on morphologically detectable local preferences, but also on further molecular biological methods. In our opinion, the main issue in IR-MSP research is currently to find stable links between spectroscopic features and clearly

defined structural and functional cellular changes, to enable IR-MSP to be used in future clinical applications.

For the first time, the tumour segment outline variation experiment demonstrates a non-homogeneous distribution of false negatives and false positives within the ROIs. The false assignment of IR data referring to the histopathological reference is mainly located in transition areas on tissue boundaries. A mixing of biochemical information of cell components and of different tissue types in these areas remains a severe problem. This result is in good accordance with previously published analyses,<sup>3,8</sup> leaving out those transition areas and focusing only on inner segment regions exhibiting well-defined tissue types, and thereby obtaining clearly higher accuracy values. Our variation experiment well illustrates the effect of such a methodical difference, which was already considered as selection bias.<sup>21</sup>

In conclusion, the IR-MSP-ascertainable differences in formalin-fixed paraffin-embedded tissue are too subtle and not specific enough for histopathological tissue discrimination for the purpose of an automated diagnosis in the strict sense. Therefore, the values of recognition accuracy found are, at present, the major limitation of the current approach. The application of this imaging technique for medical diagnostics in order to understand molecular differences associated with cell types and cell alterations is only possible in combination with concomitant conventional histopathology using transmission light microscopy. However, we expect a greater potential for more specific issues, such as the discrimination of fewer tissue types, the analysis of few substances in bio-analytical tools and biomolecular functional assays, or studies regarding sequential variances over time.

## Conflict of interest

The authors declare no conflict of interest.

## References

1. Steller W, Eienenkel J, Horn LC *et al.* Delimitation of squamous cell cervical carcinoma using infrared microspectroscopic imaging. *Anal. Bioanal. Chem.* 2006; **384**: 145–154.
2. Bhargava R. Towards a practical Fourier transform infrared chemical imaging protocol for cancer histopathology. *Anal. Bioanal. Chem.* 2007; **389**: 1155–1169.
3. Fernandez DC, Bhargava R, Hewitt SM, Levin IW. Infrared spectroscopic imaging for histopathologic recognition. *Nat. Biotechnol.* 2005; **23**: 469–474.
4. Fabian H, Thi NAN, Eiden M, Lasch P, Schmitt J, Naumann D. Diagnosing benign and malignant lesions in breast tissue sections by using IR-microspectroscopy. *Biochim. Biophys. Acta* 2006; **1758**: 874–882.
5. Chen YJ, Cheng YD, Liu HY, Lin PY, Wang CS. Observation of biochemical imaging changes in human pancreatic cancer tissue

- using Fourier-transform infrared microspectroscopy. *Chang. Gung Med. J.* 2006; **29**; 518–527.
6. Wang TD, Triadafilopoulos G, Crawford JM *et al.* Detection of endogenous biomolecules in Barrett's esophagus by Fourier transform infrared spectroscopy. *Proc. Natl Acad. Sci. USA* 2007; **104**; 15864–15869.
  7. Beljebbar A, Amharref N, Lévêques A *et al.* Modeling and quantifying biochemical changes in C6 tumor gliomas by Fourier transform infrared imaging. *Anal. Chem.* 2008; **80**; 8406–8415.
  8. Baker MJ, Gazi E, Brown MD, Shanks JH, Gardner P, Clarke NW. FTIR-based spectroscopic analysis in the identification of clinically aggressive prostate cancer. *Br. J. Cancer* 2008; **99**; 1859–1866.
  9. Isabelle M, Stone N, Barr H, Vipond M, Shepherd N, Rogers K. Lymph node pathology using optical spectroscopy in cancer diagnostics. *Spectroscopy* 2008; **22**; 97–104.
  10. Hammody Z, Argov S, Sahu RK, Cagnano E, Moreh R, Mordechai S. Distinction of malignant melanoma and epidermis using IR micro-spectroscopy and statistical methods. *Analyst* 2008; **133**; 372–378.
  11. Bird B, Romeo M, Laver N, Diem M. Spectral detection of micro-metastases in lymph node histo-pathology. *J. Biophotonics* 2009; **2**; 37–46.
  12. Khanmohammadi M, Garmarudi AB, Ghasemi K, Jaliseh HK, Kaviani A. Diagnosis of colon cancer by attenuated total reflectance-Fourier transform infrared microspectroscopy and soft independent modeling of class analogy. *Med. Oncol.* 2009; **26**; 292–297.
  13. Kelly JG, Singh MN, Stringfellow HF *et al.* Derivation of a subtype-specific biochemical signature of endometrial carcinoma using synchrotron-based Fourier-transform infrared microspectroscopy. *Cancer Lett.* 2009; **274**; 208–217.
  14. Lasch P, Haensch W, Naumann D, Diem M. Imaging of colorectal adenocarcinoma using FT-IR microspectroscopy and cluster analysis. *Biochim. Biophys. Acta* 2004; **1688**; 176–186.
  15. Bird B, Miljkovic M, Romeo MJ *et al.* Infrared micro-spectral imaging: distinction of tissue types in axillary lymph node histology. *BMC Clin. Pathol.* 2008; **8**; 8–21.
  16. Mordechai S, Sahu RK, Hammody Z *et al.* Possible common biomarkers from FTIR microspectroscopy of cervical cancer and melanoma. *J. Microsc.* 2004; **215**; 86–91.
  17. Petitbois C, Délérès G. Chemical mapping of tumor progression by FT-IR imaging: towards molecular histopathology. *Trends Biotechnol.* 2006; **24**; 455–462.
  18. Travo A, Piot O, Wolthuis R *et al.* IR spectral imaging of secreted mucus: a promising new tool for the histopathological recognition of human colonic adenocarcinomas. *Histopathology* 2010; **56**; 921–931.
  19. Baker R, Rogers KD, Shepherd N, Stone N. New relationships between breast microcalcifications and cancer. *Br. J. Cancer* 2010; **103**; 1034–1039.
  20. Krishna CM, Sockalingum GD, Vadhiraja BM *et al.* Vibrational spectroscopy studies of formalin-fixed cervix tissues. *Biopolymers* 2007; **85**; 214–221.
  21. Eienkel J, Steller W, Braumann UD, Horn LC, Krafft C. Unrealistic expectations for IR microspectroscopic imaging. *Nat. Biotechnol.* 2007; **25**; 29–31.
  22. Wolthuis R, Travo A, Nicolet C *et al.* IR spectral imaging for histopathological characterization of xenografted human colon carcinomas. *Anal. Chem.* 2008; **80**; 8461–8469.
  23. Wong PTT, Wong RK, Caputo TA, Godwin TA, Rigas B. Infrared spectroscopy of exfoliated human cervical cells: evidence of extensive structural changes during carcinogenesis. *Proc. Natl Acad. Sci. USA* 1991; **88**; 10988–10992.
  24. Yazdi HM, Bertrand MA, Wong PT. Detecting structural changes at the molecular level with Fourier transform infrared spectroscopy. A potential tool for prescreening preinvasive lesions of the cervix. *Acta Cytol.* 1996; **40**; 664–668.
  25. Walsh MJ, Singh MN, Stringfellow HF *et al.* FTIR microspectroscopy coupled with two-class discrimination segregates markers responsible for inter- and intra-category variance in exfoliative cervical cytology. *Biomark. Insights* 2008; **3**; 179–189.
  26. Chiriboga L, Xie P, Yee H *et al.* Infrared spectroscopy of human tissue. I. Differentiation and maturation of epithelial cells in the human cervix. *Biospectroscopy* 1998; **4**; 47–53.
  27. Chiriboga L, Xie P, Yee H, Zarou D, Zakim D, Diem M. Infrared spectroscopy of human tissue. IV. Detection of dysplastic and neoplastic changes of human cervical tissue via infrared microscopy. *Cell. Mol. Biol. (Noisy-le-grand)* 1998; **44**; 219–229.
  28. Wood BR, Chiriboga L, Yee H, Quinn MA, McNaughton D, Diem M. Fourier transform infrared (FTIR) spectral mapping of the cervical transformation zone, and dysplastic squamous epithelium. *Gynecol. Oncol.* 2004; **93**; 59–68.
  29. Höckel M, Horn LC, Manthey N *et al.* Resection of the embryologically defined uterovaginal (Müllerian) compartment and pelvic control in patients with cervical cancer: a prospective analysis. *Lancet Oncol.* 2009; **10**; 683–692.
  30. Wells M, Östör AG, Crum CP *et al.* Epithelial tumours of the uterine cervix. In Tavassoli FA, Devilee P eds. *World Health Organization classification of tumours. Pathology and genetics. Tumours of the breast and female genital organs.* Lyon: IARC, 2003; 259–279.
  31. Faoláin EÓ, Hunter MB, Byrne JM *et al.* Raman spectroscopic evaluation of efficacy of current paraffin wax section dewaxing agents. *J. Histochem. Cytochem.* 2005; **53**; 121–129.
  32. Pijanka J, Sockalingum GD, Kohler A *et al.* Synchrotron-based FTIR spectra of stained single cells. Towards a clinical application in pathology. *Lab. Invest.* 2010; **90**; 797–807.
  33. Wood BR, Quinn MA, Tait B *et al.* FTIR microspectroscopic study of cell types and potential confounding variables in screening for cervical malignancies. *Biospectroscopy* 1998; **4**; 75–91.
  34. Schubert JM, Bird B, Papamarkakis K *et al.* Spectral cytopathology of cervical samples: detecting cellular abnormalities in cytologically normal cells. *Lab. Invest.* 2010; **90**; 1068–1077.
  35. Papamarkakis K, Bird B, Schubert JM *et al.* Cytopathology by optical methods: spectral cytopathology of the oral mucosa. *Lab. Invest.* 2010; **90**; 589–598.

## Supporting Information

Additional Supporting Information may be found in the online version of this article:

**Table S1.** Distribution of different tissue types within the samples of the uterine cervix defined by the pathologist.

**Table S2.** Number of image pixels, number of spectra pixels, and size of all regions of interest.

Please note: Wiley-Blackwell are not responsible for the content or functionality of any supporting materials supplied by the authors. Any queries (other than missing material) should be directed to the corresponding author for the article.